In situ 3D bioprinted GDMA/Prussian blue nanozyme hydrogel with wet adhesion promotes macrophage phenotype modulation and intestinal defect repair

Yang Su [a,b], Jingyi Ju [c], Chentao Shen [c], Yanqi Li [a,b], Wangshuo Yang [a,b], Xuelai Luo [a,b], Zhenxing Wang [c], Jinhao Zeng [d,*], Lu Liu [a,b,**]

[a] *Department of Gastrointestinal Surgery Center, Tongji Hospital, Tongji Medical College, Huazhong University of Science and Technology, Wuhan, 430030, China*
[b] *Molecular Medicine center, Tongji Hospital, Tongji Medical College, Huazhong University of Science and Technology, Wuhan, 430030, China*
[c] *Department of Plastic Surgery Union Hospital Tongji Medical College Huazhong University of Science and Technology, Wuhan, 430022, China*
[d] *Department of Gastroenterology, Hospital of Chengdu University of Traditional Chinese Medicine, Chengdu, 610072, China*

ABSTRACT

Developing hydrogels with wet-adhesion, immunomodulation and regenerative repair capabilities in intestinal repair remains a formidable challenge. In the present study, the development of an anti-inflammatory, wet-adhesive, decellularized extracellular matrix hydrogel produced using three-dimensional (3D) -printing technology is presented. This hydrogel, which integrates gelatin and dopamine, was demonstrated to display excellent wet-adhesion properties, fully harnessing the outstanding regenerative potential of the decellularized small-intestine matrix. Furthermore, the integration of Prussian Blue nanozymes imparted significant anti-inflammatory and antioxidant properties. Through modulating macrophage polarization, the hydrogel was not only found to enhance tissue repair, but also to substantially mitigate inflammation. *In vivo* experiments (namely, histopathological analyses using a rat model) demonstrated that this hydrogel was able to effectively enhance tissue regeneration and healing in models of intestinal damage. In conclusion, through the utilization of 3D-printing technology, the present study has shown that the precise manufacturing and customization of the hydrogel to various shapes and sizes of intestinal defects may be executed, thereby providing an innovative strategy for intestinal repair. This advanced hydrogel has therefore been shown to hold significant promise as a bioadhesive for both emergency repair and regenerative therapy.

1. Introduction

As a common abdominal surgical intervention, colorectal surgery fulfills a crucial role in treating various abdominal diseases [1]. However, this procedure is frequently accompanied by significant challenges and postoperative complications. Among the most concerning of postoperative complications is anastomotic leakage, which occurs when the surgical repair of intestinal defects fails [2]. This condition not only complicates patient recovery, but also substantially increases the mortality rate of patients [3]. Despite sutures being the conventional method for intestinal tissue repair, these are associated with high rates of anastomotic leakage, especially in high-risk patients where the

incidence of anastomotic leakage can reach 17.6 % [4]. The limitations inherent in suturing—such as tissue damage from needle punctures and stress concentration at suture points—are key contributors to these issues [5]. Even though recent advancements in intestinal repair techniques, including the double-stapling method and stapler use, have reduced the anastomotic leakage rates, these techniques, however, are not without certain limitations, as they can cause secondary tissue damage, present technical challenges, and may not be applicable to all areas of the intestinal tract [6,7]. Therefore, the pursuit of improved methods for intestinal tissue repair remains critical.

Biological adhesives and sealants have emerged as promising alternatives or adjuncts to sutures in clinical settings [8–11]. Up to the

present time, research on gastrointestinal biological adhesives has predominantly been focused on their physicochemical properties and mechanical performance [12–14]. However, effective intestinal repair demands addressing multiple biological challenges at the same time, such as controlling inflammation, balancing immune responses and regenerating damaged tissues. Moreover, the immune system's regulatory role within the intestinal microenvironment, especially when influenced by biomaterials, is often overlooked, potentially leading to suboptimal repair outcomes. Uncontrolled inflammatory responses have been shown to disrupt intestinal homeostasis, delaying both wound healing and tissue regeneration [15,16]. On the other hand, in a separate study, a biomaterial-induced anti-inflammatory immune microenvironment was shown to enhance intestinal cell differentiation, to promote angiogenesis, and to facilitate long-term implant integration [17].

Among the key immune regulators, macrophages play a crucial role in coordinating inflammatory responses and tissue regeneration [18]. Their high plasticity allows them to transition between pro-inflammatory M1 and anti-inflammatory M2 phenotypes. Notably, M2 macrophages have been shown to improve intestinal inflammation and tissue repair through the secretion of anti-inflammatory cytokines and remodeling of the tissue environment [19]. Therefore, biomaterials that promote M2 macrophage polarization may enhance healing outcomes and contribute to more effective intestinal repair. Moreover, current biological adhesives often lack the ability to adequately remove reactive oxygen species (ROS), further complicating the healing process [20].

Inspired by mussel-adhesion mechanisms, researchers have incorporated dopamine (DA), which is structurally similar to dihydroxyphenylalanine (DOPA), into biological tissue adhesives. This innovation has effectively addressed the limitations of conventional adhesives, particularly their difficulty in bonding effectively under dynamic physiological conditions [21,22]. Small-intestinal decellularized extracellular matrix (dSI-ECM) hydrogels have attracted significant interest in tissue engineering and regenerative medicine due to their exceptional properties of biocompatibility, bioactivity, plasticity and degradability [23,24]. Nanomaterials have recently gained attention due to their small particle size, versatile applications and ease of modification [25]. Notably, Prussian Blue nanoparticles (PBNPs) have been shown to exhibit significant anti-inflammatory and antioxidant properties, proving to be effective in the treatment of inflammatory diseases such as rheumatoid arthritis and inflammatory bowel disease [26,27]. In situ 3D bioprinting is an emerging technology that allows direct deposition of biomaterials and cells at the defect site, enabling precise tissue regeneration. Compared to conventional ex vivo bioprinting followed by implantation, in situ bioprinting offers advantages such as improved cell viability, real-time adaptability to irregular defects, and the potential to reduce surgical complexity [28].

In the present study, a novel composite hydrogel material composed of dSI-ECM, gelatin, DA, methacrylic anhydride and PBNPs, which we have termed 'GEMA@PB', is presented. On the basis of this material, we propose a scalable wet-adhesive hydrogel strategy for intestinal repair. The GEMA@PB composite hydrogel that we have designed and synthesized is photosensitive, enabling high-precision 3D printing, also possessing the property of stable adhesion to biological tissues following photocuring. In addition to its adhesive properties, the GEMA@PB hydrogel facilitates immune modulation by promoting macrophage polarization from a pro-inflammatory M1 phenotype to an anti-inflammatory M2 phenotype, which plays a critical role in reducing inflammation and enhancing tissue regeneration. Moreover, its strong antioxidant capacity further aids in maintaining a favorable healing environment. Moreover, this hydrogel exhibits strong reparative and immunomodulatory capabilities. In the present study, the biocompatibility and degradability of the GEMA@PB composite hydrogel has been confirmed, both through in vitro cytotoxicity assays with human colonic epithelial cells and *in vivo* histopathological analyses and live imaging in a rat model. Additionally, using immunofluorescence and reverse

transcription-quantitative PCR (RT-qPCR) analyses, this composite hydrogel was further confirmed to promote the polarization of macrophages from a pro-inflammatory M1 phenotype to an anti-inflammatory M2 phenotype. More importantly, we validated the *in vivo* efficacy of the GEMA@PB composite hydrogel in terms of its seamlessly repairing intestinal defects in a rat colonic injury model. This innovative strategy is not only associated with a significant enhancement of the adhesive performance of hydrogel in wet environments, but it also offers a multifunctional platform that combines efficient tissue repair with immune regulation (Fig. 1). Taken together, this approach has addressed the critical need for effective and convenient intestinal defect repair, positioning this novel strategy as a promising alternative to the use of both traditional sutures and commercially available tissue adhesives.

2. Materials and methods

2.1. Preparation of GDMA

First, 10 g of gelatin was dissolved in 100 mL of phosphate-buffered saline (PBS) at 60 °C with continuous magnetic stirring. Methacrylic anhydride was then added, and the solution was stirred at 60 °C for 2 h, protected from light. The mixture was then dialyzed at 40 °C in deionized water (8–14 kDa cutoff) for 3 days to remove methacrylic acid and salts, followed by freeze-drying of the GelMA. Separately, 1 g of GelMA was dissolved in a 16 mL PBS/DMF solution (1:1, v/v). EDC (1.5 g) and NHS (0.9 g) were dissolved in 4 mL DMF, and the pH was adjusted to 5. After 30 min of stirring, GelMA carboxyl groups were activated. Dopamine hydrochloride (3 g) was dissolved in 10 mL of PBS (pH 5.0), gradually added to the activated mixture, and reacted for 12 h. The final product was dialyzed in PBS (pH 5.0) for 5 days and freeze-dried for 48 h to yield GDMA.

2.2. Preparation and characterization of dSI-ECM

Porcine small intestines were sourced from a local slaughterhouse within 4 h postmortem and immediately immersed in Hank's solution at 4 °C for transport to the laboratory. Upon arrival, the intestines were rinsed with PBS to remove residual contents and fat. Decellularization was conducted according to an optimized protocol from previous studies [29]. Briefly, the intestines were immersed in distilled water in a glass beaker and sealed for 3 h. This was followed by treatment with a 1 % Triton X-100 and 0.1 % ammonium hydroxide mixture for 48 h, and then a 24-h rinse in distilled water. The tissues were subsequently treated with a 1 % penicillin-streptomycin solution for 2 h. All steps were conducted at 4 °C with constant agitation at 180 r.p.m. The tissues were sterilized by 25 kGy γ-irradiation and stored at 4 °C until use.

To verify the efficiency of decellularization, DNA quantification and histological analyses were conducted after the process. DNA was isolated using an Animal Tissue/Cell Genomic DNA Extraction Kit following the manufacturer's protocol and quantified with the Qubit™ dsDNA Assay Kit. The GAG content was measured via the 1,9-dimethylmethylene blue dye assay following standard procedures. For histological assessments, both native and decellularized tissues were fixed in 4 % paraformaldehyde, dehydrated, embedded in paraffin, and sectioned. H&E and DAPI staining were applied for tissue visualization.

2.3. Preparation of dSI-ECM protein samples and LC-MS/MS analysis

Lyophilized samples were ground into a fine powder using a cryogenic grinder (JXFSTPRP-CLN-48, Shanghai Jingxin, China) and dissolved in lysis buffer. The mixture was kept on ice for 30 min, intermittently vortexed to ensure thorough ECM protein lysis. After lysis, the samples were centrifuged at 12,000 rpm for 15 min at 4 °C to separate insoluble components. The supernatant, containing soluble proteins, was collected for further analysis. Mass spectrometry data from three samples were acquired with a TimsTOF Pro mass spectrometer
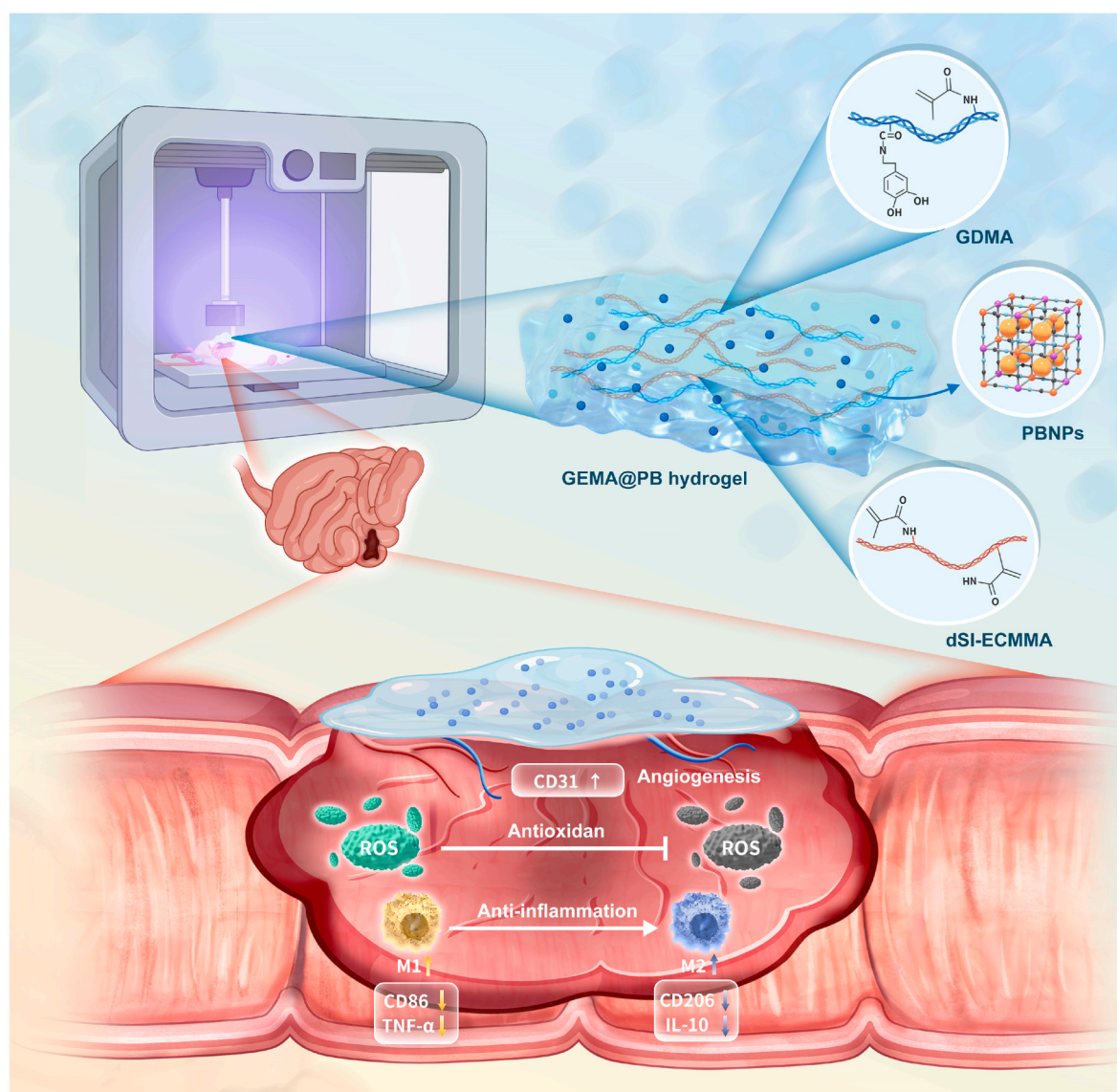
Fig. 1. Schematic synthesis of GEMA@PB hydrogel with its multifunctional characteristics, and its promising application in the healing of intestinal wounds.

(Bruker, USA) set to Data-Independent Acquisition (DIA) mode. Peptide and protein identification, along with quantification, utilized a spectral library from Data-Dependent Acquisition (DDA).

2.4. Preparation of dSI-ECMMA

To prepare the dSI-ECMMA hydrogel, 300 mg of lyophilized dSI-ECM powder was dissolved in 80 mL of 1 M acetic acid, followed by vortexing until fully dissolved. Methacrylic anhydride was then added dropwise under vigorous stirring at 4 °C. The reaction was allowed to proceed for 2 days. The resulting methacrylated ECM solution was dialyzed against deionized water at 4 °C for 7 days, using a dialysis membrane with a molecular weight cutoff of 14–16 kDa, with the water being changed twice daily. The dialyzed product was lyophilized and stored at −20 °C until further use.

2.5. Preparation and characterization of PBNPs

PBNPs were prepared by dissolving 12.375 g of $K_3Fe(CN)_6$ and 125 g of PVP in 1 L of 1 M HCl solution with magnetic stirring for 40 min to obtain a clear yellow solution. This solution was then heated at 80 °C for 20 h in an oven, yielding a blue solution containing PBNPs. The solution

was centrifuged at 14,000 rpm for 10 min to collect the precipitate, which was then resuspended in deionized water and sonicated for 10 min. This process was repeated three times. Finally, the PBNPs were collected by centrifugation, washed repeatedly with deionized water and ethanol, and stored until further analysis. The morphology of the PBNPs was observed using TEM, and their structure and elemental composition were analyzed using scanning transmission electron microscopy (STEM). FTIR spectra were recorded using a spectrophotometer (Thermo Scientific Nicolet 6700, USA) with a KBr pellet method, covering the wavelength range of 400–4000 cm^{-1}. The size of the PBNPs was measured using a dynamic light scattering analyzer (173Plus, USA).

2.6. Synthesis and characterization of GDMA, GEMA, and GEMA@PB hydrogels

A 15 % GDMA solution was prepared by dissolving lyophilized GDMA in distilled water to achieve a final concentration of 15 % (w/v). For the GEMA solution, 15 % GDMA was first prepared, followed by the addition of dSI-ECMMA at a final concentration of 2 % (w/v). The mixture was sonicated for 15 min to ensure complete mixing. For the GEMA@PB solution, GEMA was prepared as described above, and PBNPs were added at a final concentration of 100 μg/mL, followed by

20 min of sonication. The precursor solution was then mixed with 0.5 % (w/v) lithium phenyl-2,4,6-trimethylbenzoylphosphinate as a photo-initiator. FTIR measurements were performed in the frequency range of 4000-400 cm^{-1}, and the data were processed using Origin software. The morphology of the hydrogels was observed using cryo-field emission scanning electron microscopy (cryo-FESEM). Hydrogels of GDMA, GEMA, and GEMA@PB were prepared using a mold method and subjected to tensile and compressive testing using a universal testing machine (ZHIQU ZQ770, China) at a constant rate of 10 mm/min. Stress-strain curves, Young's modulus, and compression test results were analyzed using Origin software. The rheological properties of the hydrogels were evaluated using a rheometer (HAAKE RS6000, Germany) in concentric parallel plate mode, with a plate diameter of 35 mm and a gap of 1 mm.

2.7. 3D printing of GEMA@PB hydrogels

The 3D printing model was designed using Blender v4.1.1 software and converted into an STL file. A DLP 3D printer (EFL, model 8601, China) was used with the following parameters: layer thickness of 100 μm, light intensity of 10 mW/cm^2, base layer exposure time of 18 s, peel distance of 1 mm, peel speed of 100 mm/min, and peel recovery speed of 100 mm/min. After printing, the model was removed and sealed in a glass bottle at 4 °C.

2.8. Adhesion testing of GEMA@PB hydrogels

To evaluate adhesion strength, the hydrogel precursor solution was directly printed onto each substrate using in situ 3D printing, followed by gelation under the designated conditions. This approach allows the hydrogel to conform seamlessly to the substrate surface, optimizing adhesion. The lap shear strength of GDMA, GEMA, and GEMA@PB hydrogels was measured using a universal testing machine (ZHIQU ZQ770, China). Fresh porcine skin was defatted, shaved, and cut into rectangular pieces (10 × 30 mm), then soaked in PBS. The adhesion strength of the hydrogels was tested using a lap shear test.

2.9. Biocompatibility and Intra-abdominal degradation of hydrogels

Human normal colonic cells (NCM460) were seeded in 96-well plates at a density of 1×10^4 cells per well. After 24 h of incubation, sterilized hydrogels were added to the wells. The hydrogels were co-incubated with the cells for 1, 3, and 5 days. After the incubation period, the hydrogels and medium were removed, and the cells were stained according to the LIVE/DEAD cell staining kit instructions. Cell viability was observed using a confocal laser scanning microscope (OLYMPUS FV1000). Cell proliferation was assessed using the CCK8 assay. Hydrogels labeled with a fluorescent dye (EFL-DYE-UF-ENE-R, EFL, China) were prepared by adding 5 mg/mL of the dye to the GEMA@PB hydrogel precursor solution. The hydrogels were formed into circular shapes (1 cm in diameter) and applied to colonic perforations. The degradation of the hydrogels was monitored using *in vivo* small animal optical imaging (IVIS Spectrum CT, USA) at 1, 14, and 28 days.

2.10. Hemocompatibility testing of hydrogels

Red blood cells were isolated from mouse blood by centrifugation at 3000 rpm for 10 min. The separated red blood cells were washed three times with PBS buffer and then diluted to a final concentration of 2 % (w/v) in PBS. A 500 μL aliquot of hydrogel was mixed with 500 μL of the red blood cell suspension and incubated at 37 °C for 2 h. After incubation, the samples were centrifuged at 3000 rpm for 10 min, and 100 μL of the supernatant was transferred to a 96-well plate. Absorbance was measured at 540 nm using a microplate reader. Triton X-100 (0.1 %) served as the positive control, and PBS buffer was used as the negative control.

2.11. Evaluation of antioxidant activity of GEMA@PB Hydrogel In vitro and In vivo

To assess the ROS scavenging capability of the hydrogel, the experimental procedure was as follows: The prepared hydrogel samples were incubated with Fenton reagent and salicylic acid for 3 h. The hydroxyl radicals (•OH) produced reacted with salicylic acid, forming 2,3-dihydroxybenzoic acid, which was quantified by measuring the absorbance at 510 nm using a microplate reader (Synergy2, USA). In another assay, hydrogel samples were immersed in a 100 μM H$_2$O$_2$ solution, and the reaction proceeded in darkness for 3 h. The supernatant was then mixed with 2 mL Ti (SO$_4$)$_2$ solution and incubated for 30 min. Absorbance was measured at 405 nm using a microplate reader. Intracellular ROS generation was assessed using DCFH-DA as a fluorescent probe. NCM-460 cells were seeded in 12-well plates at a density of 3×10^9 cells/well and incubated for 24 h. The cells were then treated with hydrogen peroxide (100 μmol/L) with or without hydrogel for 24 h. After washing, DCFH-DA was added and incubated at 37 °C for 30 min. Fluorescence signals within the cells were observed using a confocal microscope (OLYMPUS FV1000).

2.12. In vitro evaluation of Macrophage polarization

To evaluate macrophage polarization induced by GEMA@PB hydrogels, RAW 264.7 cells were first stimulated with 1 μg/mL LPS for 24 h, then co-cultured with GEMA, GEMA@PB hydrogels, or the commercial tissue adhesive Tisseel. Briefly, RAW 264.7 cells were seeded in 6-well plates at 5×10^5 cells per well and cultured overnight. The following day, different hydrogels were added and co-cultured with the cells for 1 day. Immunofluorescence staining for M2 macrophage marker CD206 and M1 macrophage marker CD86 was performed. Cells were fixed with 4 % paraformaldehyde at 4 °C for 20 min, permeabilized with 0.1 % PBS/Triton X-100 for 5 min, and blocked with 10 % BSA/PBS for 1 h at room temperature. The cells were incubated overnight at 4 °C with primary antibodies against CD206 and CD86. After washing, Alexa Fluor® 488-conjugated goat anti-rabbit IgG secondary antibody was applied for 1 h at room temperature, and nuclei were counterstained with DAPI. Macrophage morphology was observed using a confocal laser scanning microscope, and fluorescence intensity of CD206 and CD86 was quantified using ImageJ. The expression of genes (CD86, TNF-α, CD206, and IL-10) in RAW 264.7 cells after hydrogel treatment was analyzed by qRT-PCR, using primers listed in Supplementary Table 1.

2.13. In vivo wound healing assessment using a colon defect model

All animal experiments were performed following the guidelines of the Animal Care and Use Committee of Huazhong University of Science and Technology. Male Sprague Dawley (SD) rats were chosen for the study, with female rats excluded to reduce potential hormonal effects on the outcomes. The rats, aged 8 weeks and weighing 220–240 g, were acclimatized for one week before surgery. Anesthesia was induced by intraperitoneal injection of 1.25 % avertin at a dosage of 10 ml/kg body weight. A midline incision was made to access the abdominal cavity, and a 5 mm full-thickness perforating wound was created in the colon using a punch. The rats were randomly divided into four groups: untreated group, suture-only group, GEMA hydrogel group, and GEMA@PB hydrogel group, with 9 rats per group. Wound healing was monitored and documented using a digital camera over a 4-week period.

2.14. Histological and immunofluorescence analysis

Four weeks post-surgery, intestinal tissue samples were collected, fixed, paraffin-embedded, and sectioned. Sections were stained with H&E and Masson's trichrome to assess tissue regeneration and collagen deposition. On days 3 and 7 post-surgery, samples were stained with CD31, CD86, CD206, and DAPI to evaluate macrophage infiltration and

polarization. In brief, for immunostaining, tissue sections were deparaffinized and subjected to antigen retrieval, followed by PBS washing and 15 min of buffer wash. The samples were incubated with 10 % goat serum for 1 h to block non-specific binding and then incubated overnight at 4 °C with the respective primary antibodies. After washing the primary antibodies, sections were incubated with the corresponding secondary antibodies and DAPI staining. Samples were imaged using an inverted fluorescence microscope.

2.15. RNA transcriptome analysis

On day 3 post-modeling, tissue samples were collected from the intestinal region of rats in both the suture and GEMA@PB groups following the same protocol. The intestinal tissues were placed in freezing vials, rapidly frozen in liquid nitrogen for 5 min, and stored at −80 °C until further sequencing. The samples were sent to Wuhan Baiyihui Energy Biotechnology Co. (Wuhan, China) for transcriptome sequencing and analysis.

2.16. Statistical analysis

All experimental data were derived from a minimum of three independent experiments and are presented as mean $\pm$ standard deviation (SD). For comparisons between two groups, a Student's t-test was performed, while multiple group comparisons were assessed using analysis of variance (ANOVA) followed by Tukey's post hoc test. A P-value of less than 0.05 was considered statistically significant.

3. Results

3.1. Preparation and characterization of dSI-ECM

Fig. 2A depicts the preparation workflow of dSI-ECM. Compared to the untreated control group, H&E and DAPI staining showed no significant residual cell nuclei in the dSI-ECM, confirming the successful removal of cellular components while preserving the structural integrity of the extracellular matrix (Fig. 2B). Quantitative DNA analysis before and after decellularization revealed a substantial reduction in DNA content, with post-treatment levels consistently below 50 ng/mg (38.53 $\pm$ 3.50 ng/mg), representing an average reduction of over 85 %, thereby demonstrating the high efficiency of the decellularization process (Fig. 2C). To assess the impact of decellularization on glycosaminoglycan (GAG) content in the intestinal matrix, we performed quantitative analysis using dimethylmethylene blue (DMMB) staining. The results indicated that while GAG content was reduced compared to untreated intestinal samples, it remained relatively high, with approximately 46.8 % of the original content retained. This suggests that essential bioactive components such as GAGs were well-preserved despite the removal of most cellular and cell-associated materials (Fig. 2D).

3.2. Proteomic analysis of dSI-ECM

To investigate the composition of the ECM after decellularization, mass spectrometry was performed on the powdered ECM. This analysis identified over 1500 proteins, including 123 specifics to the ECM and 238 related to extracellular exosomes (Fig. 2E), highlighting the ECM's dual function as both a structural scaffold and a reservoir for soluble signaling molecules. The most abundant ECM proteins identified were COL6A1, COL6A2, COL6A3, LAMC1, and COL1A1, underscoring their critical roles in ECM architecture (Fig. 2F). Variations among three different dSI-ECM samples were evaluated, with pie charts and bar graphs illustrating the distribution of ECM components, including collagens, glycoproteins, proteoglycans, ECM regulators, and secreted factors. Notably, collagen consistently emerged as the most abundant protein category across all samples, followed by glycoproteins and ECM

regulators (Fig. 2G). Principal component analysis (PCA) and correlation analysis revealed clustering among the three dSI-ECM samples, indicating a high degree of consistency in their protein compositions (Fig. 2H and I). Gene Ontology (GO) analysis further indicated that the dSI-ECM proteins are enriched in biological processes, including cell adhesion, differentiation, migration, and extracellular matrix organization, reflecting their structural and functional significance in the small intestine (Fig. 2J).
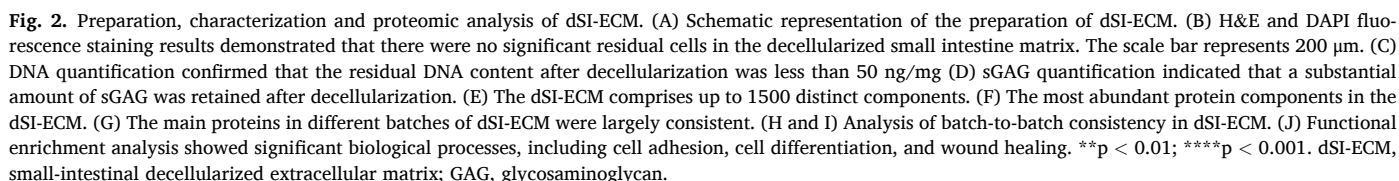
3.3. PBNPs preparation and characterization

In this study, polyvinylpyrrolidone (PVP)-modified PBNPs were synthesized using a simple hydrothermal method, as previously reported [30] (Fig. 3A). Scanning electron microscopy (SEM) analysis revealed that the PBNPs exhibit highly uniform cubic morphologies with an average particle size of approximately 102.5 nm (Fig. 3B–D). Elemental mapping confirmed the even distribution of Fe, C, and N within the PBNP structure (Fig. 3E–H). X-ray diffraction (XRD) revealed the alignment of the PBNPs crystal structure with the standard PBNPs pattern, demonstrating precise control over the synthesis process and high product purity (Fig. 3I). Fourier-transform infrared (FTIR) spectroscopy identified characteristic absorption peaks of PBNPs, including a prominent peak at 2088 cm^{-1} corresponding to the stretching vibration of -C $\equiv$ N- in Fe^{2+}-CN-Fe^{3+}, and a broad peak at 3415 cm^{-1} associated with the O-H stretching vibration. Additionally, absorption peaks near 590 cm^{-1} and 420 cm^{-1}, associated with Fe-C and Fe-N vibrational modes, respectively, further validated the bonding characteristics within the PBNPs lattice (Fig. 3J). Dynamic light scattering (DLS) measurements indicated a concentration peak at 110.5 nm, reflecting the size distribution of the PBNPs in solution (Fig. 3K).

3.4. Characterizations of GEMA@ PB hydrogels

Methacrylic anhydride (MA) primarily modifies the dSI-ECM by reacting with amino residues in proteins. FTIR spectroscopy revealed a bending vibration peak of C-H in alkenes at 970 cm^{-1} in dSI-ECMMA, confirming the successful synthesis of dSI-ECMMA (Fig. S1). MA further reacts with amino groups in gelatin, yielding GelMA. Subsequently, dopamine's amino group binds with the activated carboxyl group on GelMA, forming GDMA. The structures of gelatin, GelMA, GDMA, and DA were confirmed through FTIR spectroscopy (Fig. S2). GDMA was then mixed with dSI-ECMMA to create a homogeneous aqueous solution. Upon the addition of PBNPs and exposure to UV light, the solution undergoes crosslinking to form a GEMA@PB composite hydrogel. FTIR spectroscopy revealed characteristic peaks corresponding to both GEMA and PB in the GEMA@PB composite hydrogel (Fig. 4A). SEM images of the hydrogels (Fig. 4B) reveal that all samples possess a three-dimensional porous structure in their lyophilized state. The porous structure of GEMA@PB and GEMA hydrogels is denser and more uniform than that of GDMA hydrogels. This improved structural uniformity is attributed to the abundant collagen and other matrix proteins in dSI-ECMMA, which effectively fill the larger pores, resulting in a more refined porous structure. The improved uniformity contributes to the increased mechanical strength of the hydrogels.

To assess the mechanical properties of the hydrogels, rectangular samples (0.7 mm in height and 9 mm in width) were prepared and subjected to tensile testing. The results showed that GEMA@PB exhibited the highest tensile strain, while GDMA exhibited the lowest. The inclusion of PBNPs significantly increased Young's modulus of the hydrogels compared to GDMA and GEMA (Fig. 4C and D). Furthermore, cylindrical hydrogel samples (6 mm in diameter and height) were subjected to compression testing. The results demonstrated that the elastic modulus of GEMA@PB was significantly higher than that of GDMA and GEMA, indicating that GEMA@PB hydrogels possess superior resilience under compression (Fig. 4E). Dynamic oscillatory rheology tests revealed that in the low frequency range, the storage modulus (G′)
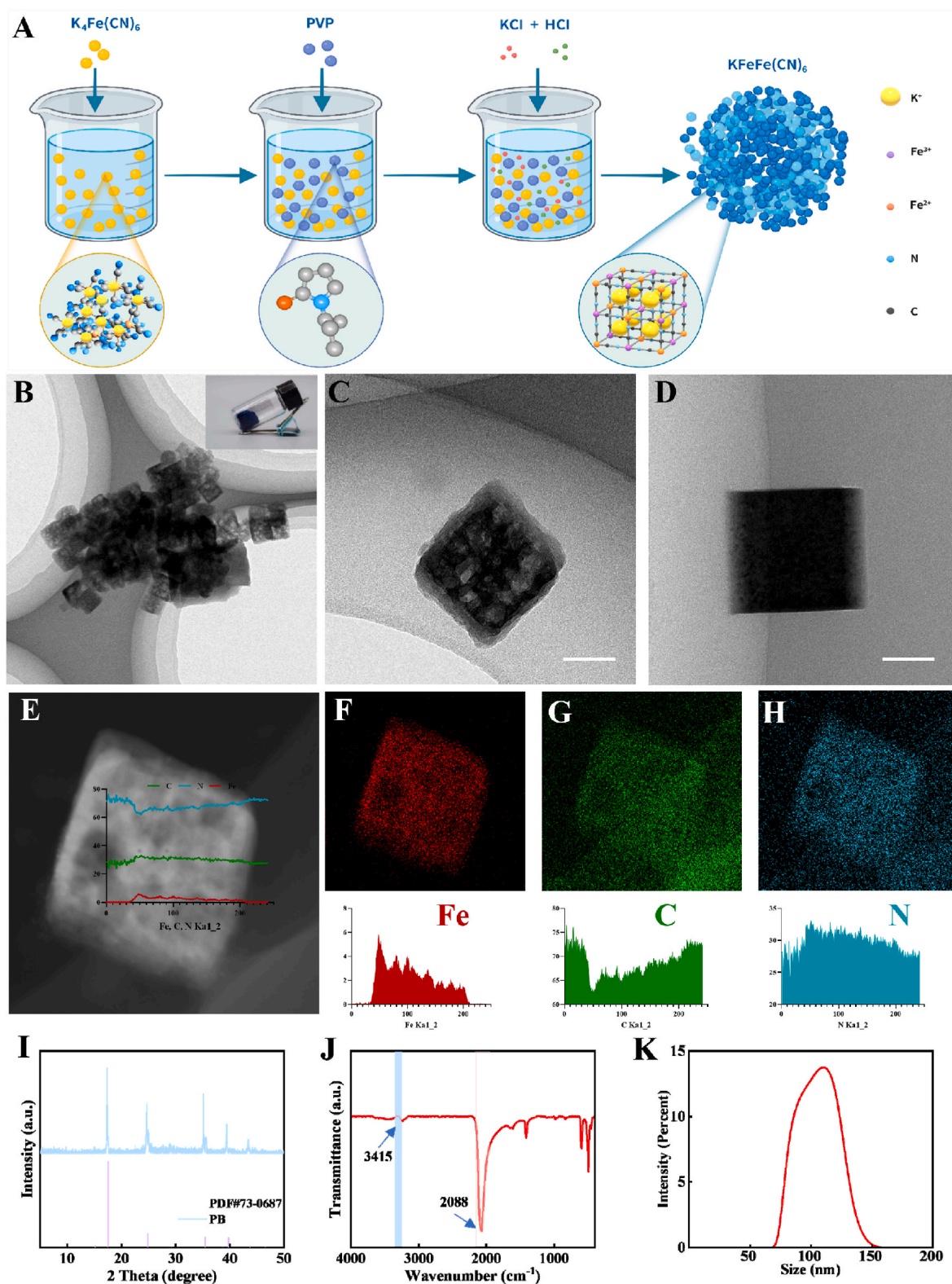
Fig. 2. Preparation, characterization and proteomic analysis of dSI-ECM. (A) Schematic representation of the preparation of dSI-ECM. (B) H&E and DAPI fluorescence staining results demonstrated that there were no significant residual cells in the decellularized small intestine matrix. The scale bar represents 200 μm. (C) DNA quantification confirmed that the residual DNA content after decellularization was less than 50 ng/mg (D) sGAG quantification indicated that a substantial amount of sGAG was retained after decellularization. (E) The dSI-ECM comprises up to 1500 distinct components. (F) The most abundant protein components in the dSI-ECM. (G) The main proteins in different batches of dSI-ECM were largely consistent. (H and I) Analysis of batch-to-batch consistency in dSI-ECM. (J) Functional enrichment analysis showed significant biological processes, including cell adhesion, cell differentiation, and wound healing. **$p < 0.01$; ****$p < 0.001$. dSI-ECM, small-intestinal decellularized extracellular matrix; GAG, glycosaminoglycan.

Fig. 3. Preparation and characterization of the PBNPs. (A) Diagram illustrating the PBNPs synthesis procedure. (B) TEM revealed that the average nanoparticle diameter of PBNPs was 102.5 nm. (C and D) High-magnification TEM images of the PBNPs are shown. The scale bar represents 50 nm. (E) STEM analysis of PBNPs. (F–H) Elemental mapping of PBNPs using EDS analysis, with corresponding intensity profiles of Fe, C, and N displayed below, confirming the elemental composition of PBNPs. (I) XRD patterns of PBNPs, matching with standard PBNPs pattern, confirming the crystalline structure of PB. (J) FTIR spectrum of PBNPs, showing characteristic peaks at 3415 cm^{-1} and 2088 cm^{-1}. (K) DLS analysis of PBNPs, indicating an average particle size distribution around 110.5 nm. PBNPs, Prussian Blue nanoparticles; TEM, transmission electron microscopy; STEM, scanning TEM; XRD, X-ray diffraction; FTIR, Fourier transform-infrared; DLS, dynamic light scattering. (For interpretation of the references to color in this figure legend, the reader is referred to the Web version of this article.)
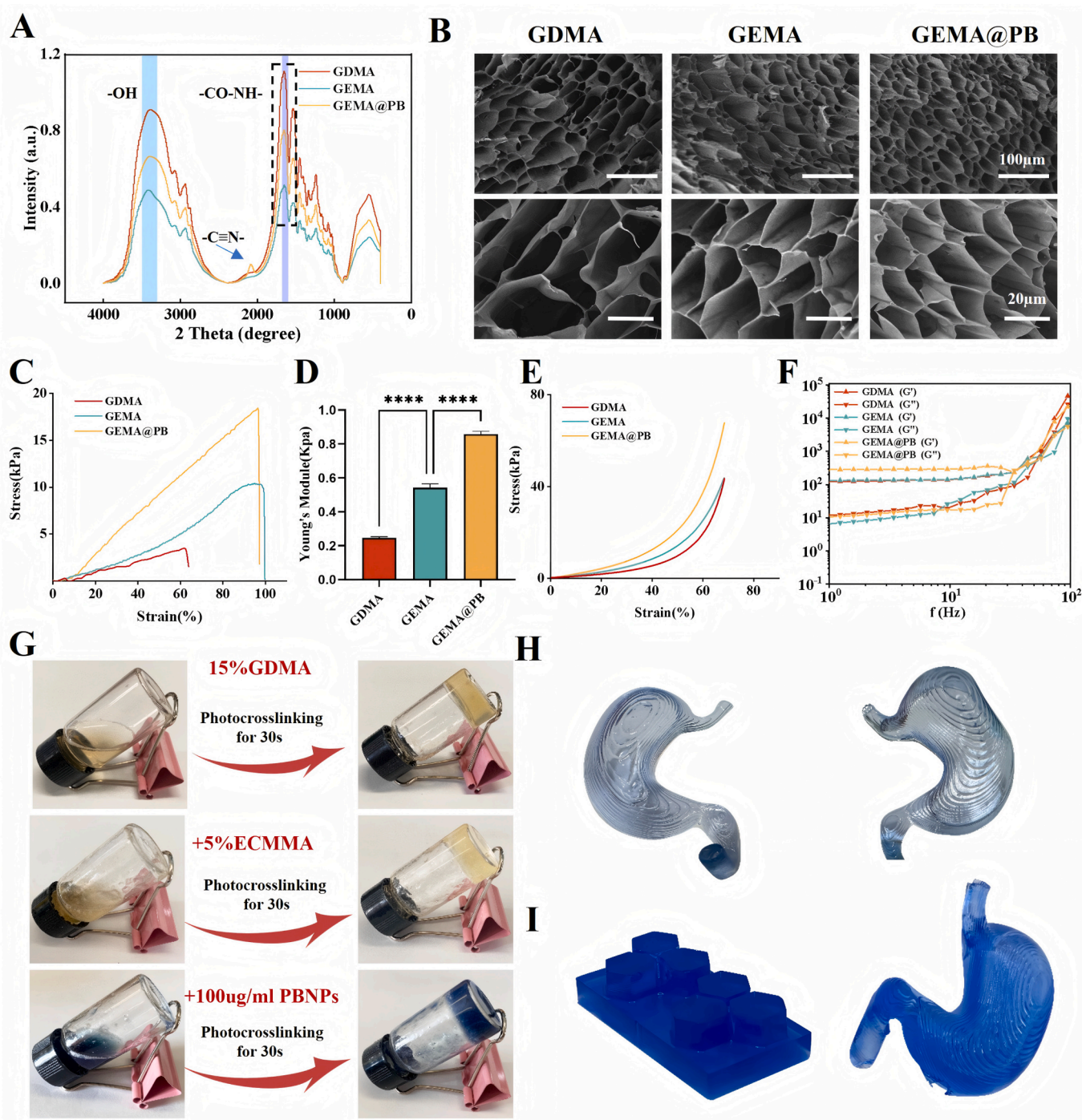
Fig. 4. Characterization of the GEMA@PB hydrogel. (A) FTIR spectroscopy revealed characteristic peaks corresponding to both GEMA and PB in the GEMA@PB composite hydrogel. (B) SEM images indicated that the pore size of the hydrogel decreased with the incorporation of dSI-ECMMA and PB. (C) The tensile stress-strain curves, demonstrating enhanced mechanical properties of GEMA@PB. (D) Young's modulus of the hydrogels, indicating significantly higher stiffness for GEMA@PB. (E) Compression stress-strain curve analysis, showing better resilience in GEMA@PB. (F) Rheological tests demonstrate the printability of GDMA, GEMA, and GEMA@PB. (G) Stepwise photopolymerization process of hydrogels with varying compositions. (H) 3D-printed models of the left and right stomach using hydrogel formulations containing 50 μg/mL PBNPs. (I) Hydrogel formulations with 100 μg/mL PBNPs demonstrate the versatility of GEMA@PB hydrogels in creating stomach and hepatic sinusoid shapes. ****$p < 0.001$. SEM, scanning electron microscopy; FTIR, Fourier transform-infrared.

surpassed the loss modulus (G''), suggesting predominantly solid-like behavior, enabling the hydrogels to maintain their shape. At higher frequencies, G' and G'' values were similar, indicating that the GDMA, GEMA and GEMA@PB can adapt to dynamic conditions during the printing process (Fig. 4F). Fig. 4G illustrates the molding effects of GDMA hydrogels following the addition of different functional components (dSI-ECMMA and PBNPs). Photopolymerization allowed these

materials to rapidly form stable hydrogel structures with controlled physical properties and color. Utilizing DLP printing technology, precise models of the stomach and liver sinusoids were successfully printed (Fig. 4H and I). The release profile of PBNPs from the GEMA@PB hydrogel shows a rapid initial release within the first three days, followed by a sustained release phase that gradually reaches approximately 90 % cumulative release by day 8. This suggests that hydrogel provides a

controlled and sustained release of PBNPs, which may contribute to prolonged therapeutic effects (Fig. S4).

3.5. Adhesive properties, biocompatibility, biodegradability and oxidation resistance of GEMA@PB hydrogels

Hydrogels containing phenolic hydroxyl groups have been reported to adhere to various substrates through hydrogen bond formation [31]. Fig. 5A presents a mechanistic diagram illustrating hydrogel adhesion to the intestinal tract. In this study, we observed that GEMA@PB hydrogels exhibited strong adhesion to a wide range of materials. As shown in Fig. 5B, GEMA@PB hydrogels adhered effectively to biological tissues, including the heart, liver, spleen, lung, kidney, and pig skin. Additionally, the hydrogels also adhered to a variety of organic and inorganic materials, such as polypropylene, glass, wood, and iron, without any surface pretreatment. To ensure optimal adhesion, all hydrogels in this study were formed in situ directly on the respective substrates rather than being pre-formed and subsequently applied. This in situ formation promotes intimate contact between the hydrogel and the substrate, enhancing adhesion strength. Adhesive strength was evaluated using lap shear. In the lap shear test, the adhesive strengths for GDMA, GEMA, and GEMA@PB was $13.71 \pm 0.53, 12.66 \pm 0.52$ and 12.27 ± 0.31, respectively (Fig. 5C). The results indicate that the incorporation of dSI-ECMMA and PBNPs does not significantly alter the adhesive properties of GDMA hydrogels. An *in vivo* peritoneal degradation test revealed that the hydrogel remained stable for more than 2 weeks and gradually degraded completely by 4 weeks (Fig. 5D).

Biocompatibility is crucial for biohydrogel adhesives. The cytotoxicity of GEMA@PB hydrogel was evaluated using the Cell Counting Kit-8 (CCK 8) assay and Live/Dead staining. NCM460 cells cultured with hydrogels for 5 days exhibited nearly threefold proliferation (Fig. 5F). Subsequently, Live/Dead staining was also used to assess cytotoxicity, where green and red fluorescence represent live and dead cells, respectively. As observed in Fig. 5E, minimal red fluorescence was detected in the hydrogel-treated groups. We further assessed the *in vivo* biocompatibility of GEMA@PB hydrogel by examining the heart, liver, spleen, lungs, and kidneys 2 weeks after hydrogel implantation. H&E staining was used to detect host inflammatory responses to the hydrogel, and no significant inflammation was observed in any of the organs (Fig. S3). The hemolysis test results showed that the hemolysis rates in the GDMA, GEMA, and GEMA@PB hydrogel treatment groups were all below 3 %, indicating that the hydrogels exhibit very low hemolytic activity (Fig. 5G). Based on these results, we can conclude that GEMA@PB hydrogel is safe for *in vivo* applications. Fig. 5H and I demonstrates the antioxidant capacity of GEMA@PB hydrogels in scavenging free radicals, specifically -OH and H_2O_2. Compared to GDMA and GEMA hydrogels, GEMA@PB hydrogels showed significantly higher scavenging efficiency, with average scavenging rates for -OH and H_2O_2 over a 3-h period reaching approximately 38.2 % and 61.2 %, respectively. Fig. 5I further highlights the protective effect of GEMA@PB hydrogels against oxidative stress in NCM460 cells. Cells exposed to 100 μmol/L H_2O_2 (control group) exhibited strong ROS signals, as indicated by the green fluorescence of the DCFH-DA probe. However, cells treated with GEMA@PB hydrogels showed a significant reduction in ROS levels, demonstrating the hydrogels' potent antioxidant capability. Although GDMA and GEMA hydrogels also reduced ROS levels, the effect was less pronounced compared to GEMA@PB, further underscoring the superior efficacy of GEMA@PB hydrogels in mitigating oxidative damage.

3.6. In vitro macrophage phenotype modulation by GEMA@PB hydrogels

Macrophages are key players of the innate immune system, playing pivotal roles in host protection, immune response regulation, and wound healing promotion [32]. In this study, we conducted in vitro co-culture experiments to evaluate the ability of GEMA@PB hydrogel to shift macrophage polarization from the pro-inflammatory M1 phenotype to

the anti-inflammatory M2 phenotype (Fig. 6A). Immunofluorescence staining was used to assess macrophage polarization by identifying surface markers CD86 (M1) and CD206 (M2). Compared with the GEMA, LPS, and Tisseel groups, macrophages treated with GEMA@PB hydrogel displayed more elongated morphologies and prominent pseudopodial extensions (Fig. S5 and Fig. 6B). The GEMA@PB hydrogel group exhibited the highest positive staining for CD206, followed by the GEMA and control groups, while the GEMA@PB group showed the least positive staining for CD86, consistent with statistical analyses (Fig. 6C and D). Additionally, the GEMA@PB hydrogel group significantly upregulated M2 markers CD206 and IL-10, and downregulating M1 markers CD86 and TNF-α, compared to the LPS and GEMA groups (Fig. 6E). These findings indicate that GEMA@PB hydrogel effectively induces macrophage polarization from the M1 to the M2 phenotype, encouraging a shift from pro-inflammatory to anti-inflammatory cytokine production.

3.7. GEMA@PB hydrogel enhances the healing of damaged intestines

To assess the therapeutic efficacy of GEMA@PB hydrogel in treating intestinal perforations, we used it as a tissue adhesive in a rat model (Fig. 7A and B). As illustrated in Fig. 7C, a 0.5 cm perforation was created in the rat intestine using a punch, followed by treatment with GEMA@PB hydrogel patches, GEMA hydrogel, and sutures. In the hydrogel-treated groups, the perforation was gently cleansed with a cotton swab and quickly sealed with a 1 cm hydrogel patch. The repaired intestinal tissues were analyzed using H&E and Masson's trichrome staining. H&E staining revealed effective healing of the incisions in the GEMA@PB and GEMA hydrogel-treated groups 4 weeks post-surgery, showing smooth intestinal surfaces with no signs of tissue adhesion. In contrast, the suture group exhibited severe tissue adhesion, likely due to intestinal fluid leakage and an associated inflammatory response (Fig. 7D). Masson's trichrome staining further demonstrated enhanced collagen deposition in the GEMA@PB group at 4 weeks, indicating superior wound healing efficiency (Fig. 7E).

3.8. Potential regulatory mechanism of intestinal injury repair microenvironment by GEMA@PB hydrogel

The study identifies the initial three days following injury as the critical period for modulating the local microenvironment of tissue defect sites [33]. To explore the underlying mechanism by which GEMA@PB hydrogel controls inflammation *in vivo*, RNA sequencing (RNA-seq) analysis was conducted on samples from both the GEMA@PB hydrogel group and the control group. The RNA-seq data demonstrated high quality, meeting all required standards. Unsupervised PCA revealed distinct genomic profiles in the repair of intestinal injury between the GEMA@PB hydrogel group and the control group (Fig. 8A). Based on the criteria of |log2 fold change| > 1 and P-value <0.05, we identified 925 differentially expressed genes between the two groups, with 559 genes upregulated and 366 genes downregulated (Fig. 8B). GO classification of these differentially expressed genes highlighted significant variations in biological processes (BP), cellular components (CC), and molecular functions (MF), particularly in immune response, inflammatory response, cytokine activation, chemotaxis, extracellular region, and protein degradation (Fig. 8C). These genes are closely associated with the interaction with the immune environment during intestinal regeneration. KEGG pathway analysis further revealed that the differential gene sets were implicated in inflammation-related pathways, including cytokine-cytokine receptor interaction, NOD-like receptor signaling, TNF signaling, IL-17 signaling, and chemokine signaling pathways (Fig. 8D–F). The results of gene set enrichment analysis (GSEA) further showed that GEMA@PB hydrogel treatment induced TH17 cell differentiation and intestine immune network for IgA production (Fig. 8G and H). This suggests that the hydrogel may play a role in regulating mucosal immunity, potentially by modulating macrophage polarization toward
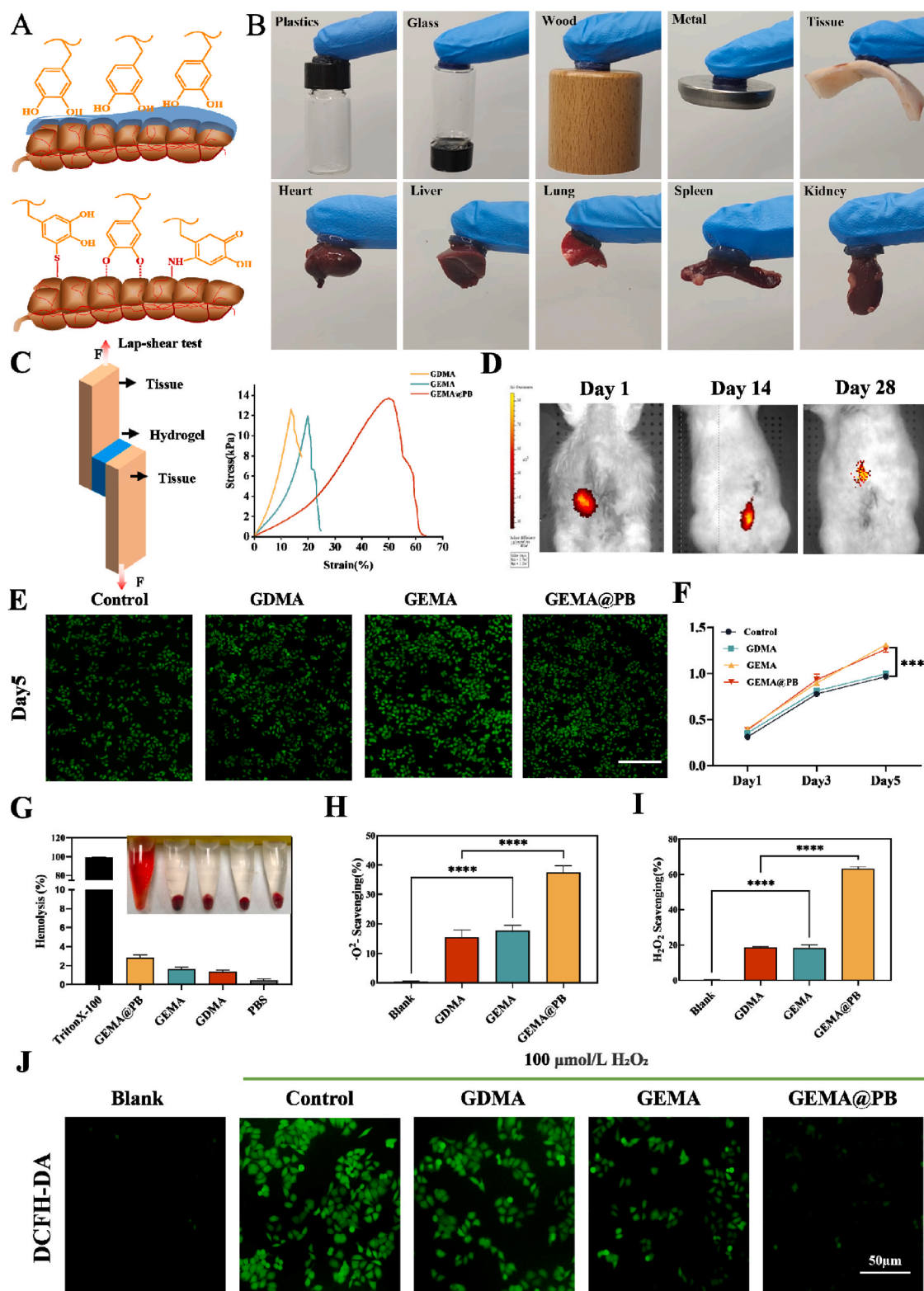
Fig. 5. Adhesive properties of the GEMA@PB hydrogels. (A) Schematic illustration of GEMA@PB hydrogel adhesion to intestinal tissue, demonstrating effective attachment to biological surfaces. (B) Adhesion of hydrogels to various materials, including plastic, glass, wood, metal, and tissues (heart, liver, lung, spleen, and kidney). (C) Lap-shear test, showing enhanced adhesion properties of GEMA@PB. (D) *In vivo* imaging of GEMA@PB labeled with the fluorescent dye, EFL-DYE-UF-ENE-R, and (E) Live/Dead staining of NCM460 cells cultured on hydrogels confirmed the biocompatibility and safety of the hydrogels. The scale bar represents 200 μm. (F) The CCK-8 assay demonstrated that the incorporation of dSI-ECMMA effectively promotes cell proliferation. (G) Hemolysis test results indicating the hemocompatibility of the hydrogels, with images of test tubes demonstrating blood compatibility. (H–I) Hydrogel scavenging efficiency against -OH and H_2O_2 is shown. (J) Fluorescence microscopy images of intracellular ROS levels using DCFH-DA staining, indicating ROS in NCM460 cells cultured on GEMA@PB hydrogels. The scale bar represents 50 μm. CCK-8, Cell Counting Kit-8; ROS, reactive oxygen species.
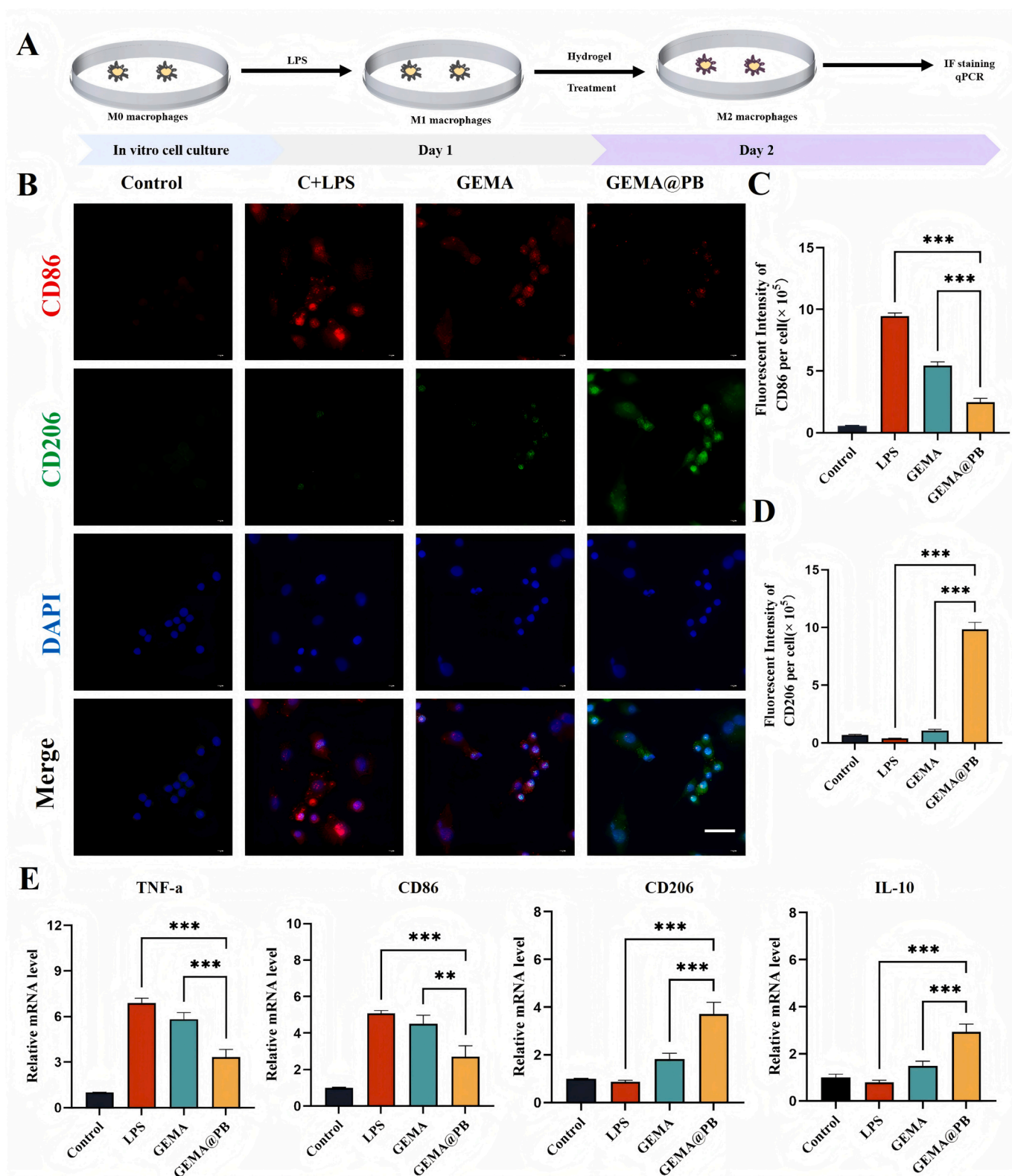
Fig. 6. The GEMA@PB hydrogel stimulates the polarization of RAW264.7 macrophages from the M1 phenotype to the M2 phenotype. (A) A Schematic representation of the macrophage polarization induction process. (B) Representative images of CD206 and CD86 staining in macrophages on day 2 are shown. The scale bar represents 50 μm. (C and D) Quantitative analysis of the fluorescence intensity for CD206 and CD86 is shown. (E) The relative mRNA expression levels of CD86, CD206, IL-10, and TNF-α in macrophages from different groups demonstrate that the GEMA@PB hydrogel effectively induces macrophage polarization from the M1 to the M2 phenotype. **$p < 0.01$; ***$p < 0.001$. IL-10, interleukin-10; TNF-α, tumor necrosis factor-α.
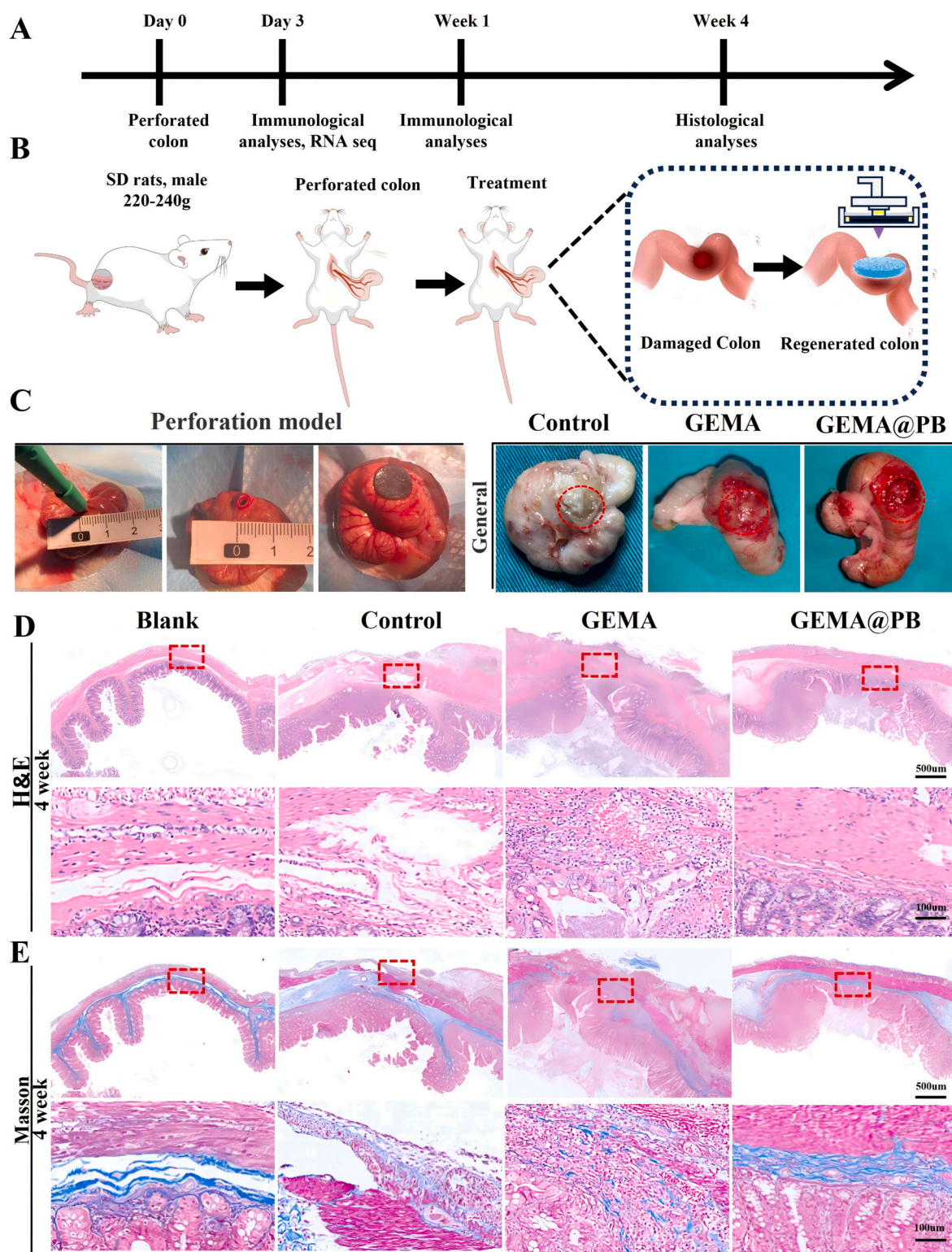
Fig. 7. Histological analysis of the hydrogel 4 weeks after perforation surgery. (A and B) Schematic diagram of the surgical process. (C) Colon perforation modeling and gross images at 4 weeks, showing significant inflammatory hyperplasia in the suture group. (D and E) Representative H&E and Masson staining images of wound samples from different groups at 4 weeks, demonstrating the superior wound healing efficiency of GEMA@PB.

an M2 phenotype, reducing oxidative stress, and fostering a favorable immune environment for IgA class switching and secretion. Given the established role of IgA in intestinal homeostasis and barrier protection, these findings further highlight the immunomodulatory potential of GEMA@PB hydrogel in intestinal repair. Additionally, a PPI network was constructed using the STRING database to shed light on the

molecular mechanisms of GEMA@PB hydrogel in intestinal injury repair (Fig. 8I). To delve deeper into the cellular mechanisms, immunofluorescence staining was performed. Quantitative analysis at days 3 and 7 post-injury indicated that, compared to the control group, the GEMA@PB hydrogel group exhibited reduced expression of the macrophage-associated M1 marker CD86, while expression of the M2
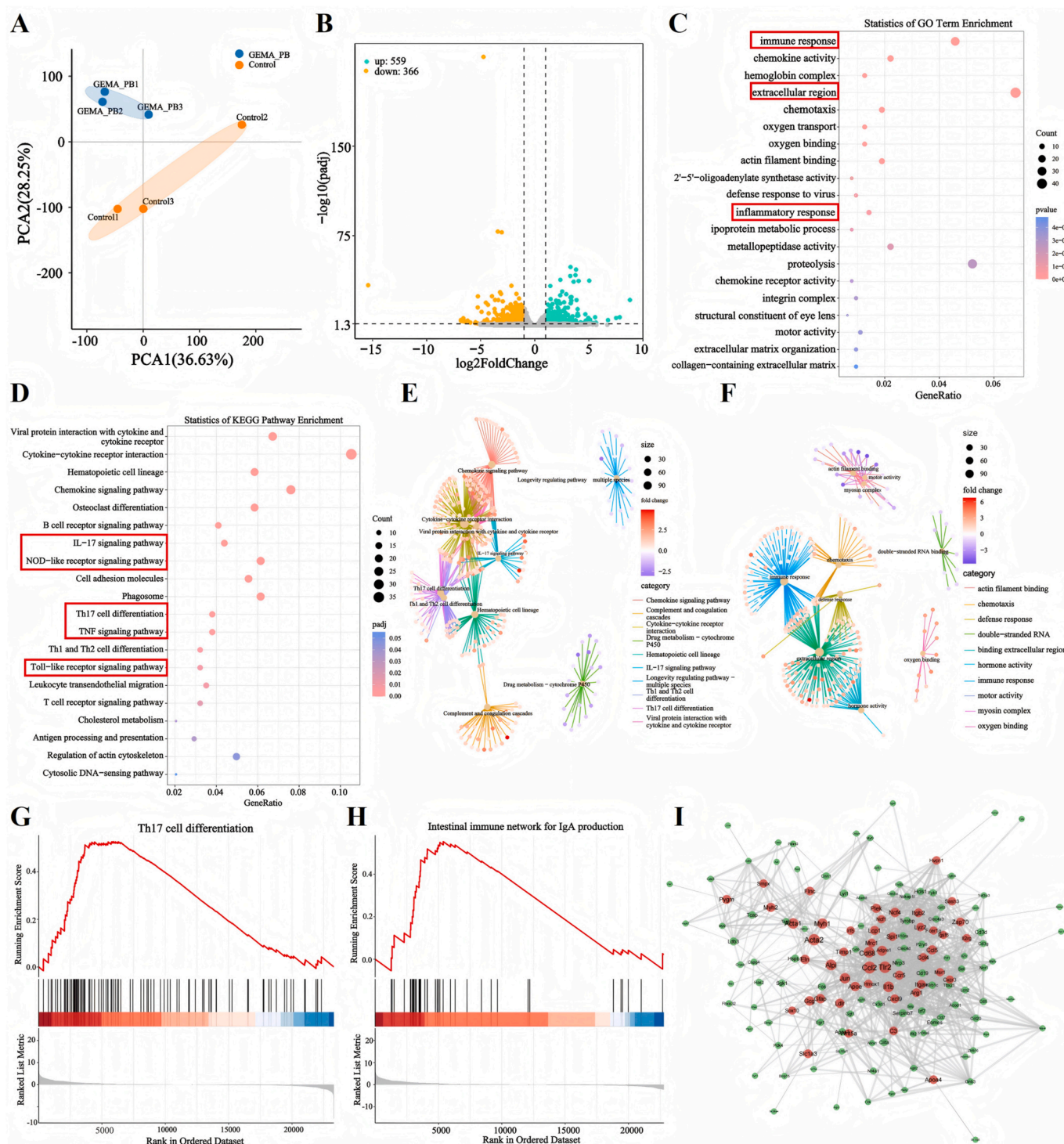
Fig. 8. Regulatory mechanism of the effect of multifunctional composite hydrogels on the localized intestinal regenerative microenvironment. (A) PCA plot showing the distribution of samples treated with GEMA-PB compared to control, highlighting significant variance along the principal components. (B) Volcano plot illustrating differentially expressed genes, with 559 upregulated and 365 downregulated genes in the GEMA@PB group. (C)GO enrichment analysis, highlighting significant terms such as immune response, extracellular region, and inflammatory response. (D) KEGG pathway enrichment analysis, showing key pathways involved, including NF-κB signaling, Th17 cell differentiation, and TNF signaling. (E and F) Visualization of GO and KEGG term networks, illustrating enriched pathways and functional interactions. (G and H) GSEA results for Th17 cell differentiation and intestinal immune network for IgA production pathways, showing enrichment in the GEMA@PB group. (I) PPI network of differentially expressed genes, highlighting key regulatory nodes. PCA, principal component analysis; GO, Gene Ontology; Kyoto Encyclopedia of Genes and Genomes; GSEA, gene set enrichment analysis; PPI, protein-protein interaction.

marker CD206 was enhanced (Fig. 9A and C). Moreover, evaluation of CD31 expression at 7 days postoperatively demonstrated that the GEMA@PB hydrogel group showed the most significant neo-vascularization (Fig. 9B and E).

4. Discussion

In tissue engineering and regenerative medicine, developing multi-functional biomaterials for effective intestinal repair and regeneration
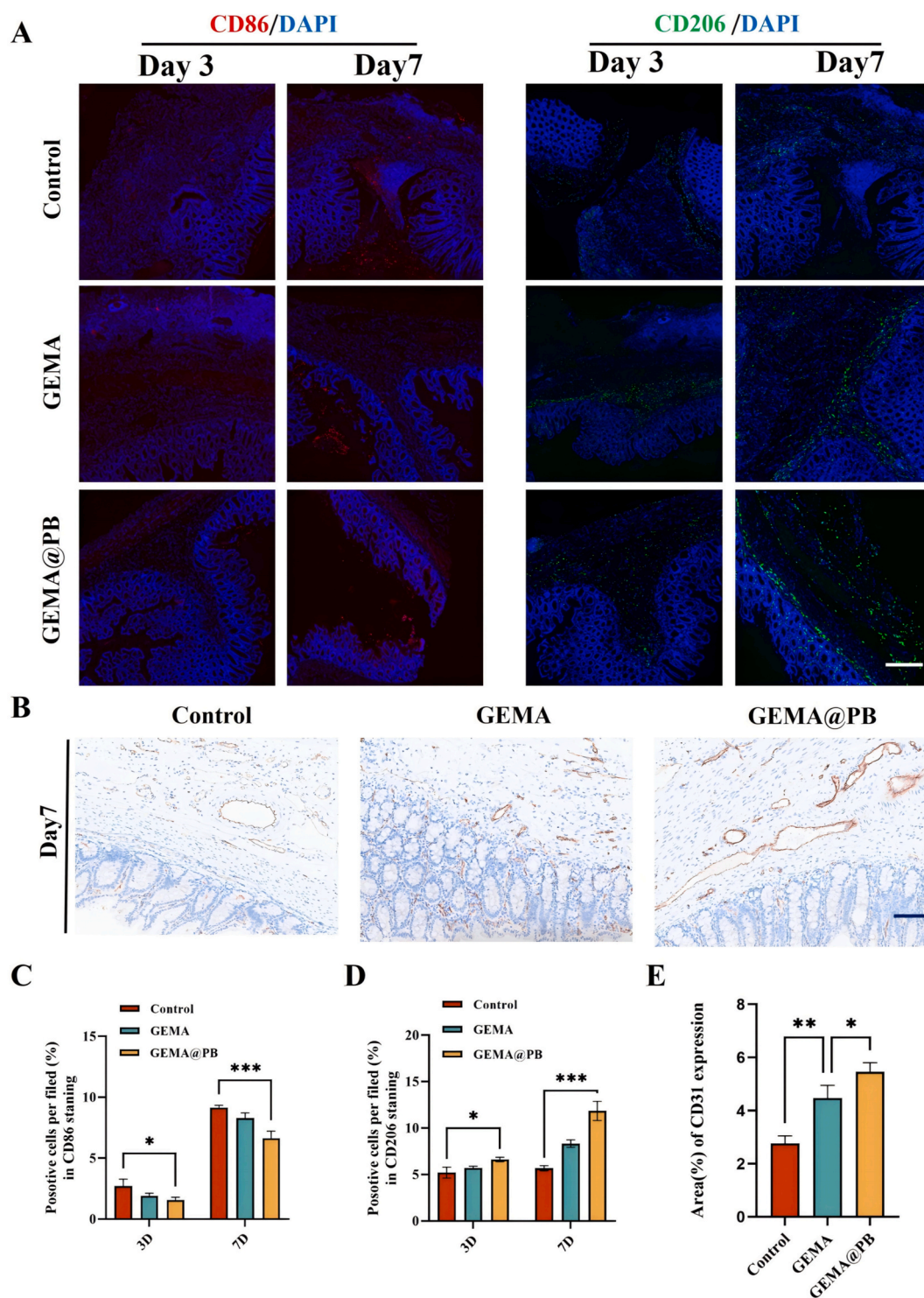

Fig. 9. Immunofluorescence staining results for CD206 and CD86 in wound samples on days 3 and 7, and angiogenesis on day 7. (A) Representative images of CD206 and CD86 immunofluorescence staining in all groups are shown. The scale bar represents 100 μm. (B) Representative images of CD31 immunohistochemical staining in all groups are shown. The scale bar represents 200 μm. (C) Quantification of CD86-positive cells (M1 macrophages) per field at days 3 and 7, showing a decrease in GEMA@PB compared to control and GEMA groups. (D) Quantification of CD206-positive cells (M2 macrophages) per field at days 3 and 7, with significantly higher levels in the GEMA@PB group. (E) CD31 expression area percentage, indicating enhanced vascularisation in the GEMA@PB group compared to control and GEMA groups. *p < 0.05; ***p < 0.001.

remains a significant challenge. Intestinal wound healing, especially in the colon, is a complex, multi-stage process that encompasses hemostasis, inflammation, proliferation and matrix remodeling, with inflammation fulfilling a pivotal role throughout [34]. Persistent inflammation, often caused by the infiltration of inflammatory cells and the upregulation of pro-inflammatory cytokines, may markedly delay the healing process [35]. Moreover, during intestinal repair, excessive levels of ROS and insufficient angiogenesis occasionally lead to the disruption of glucose metabolism and collagen deposition, leading to increased cytotoxicity and prolonged healing [36]. Regarding current materials used for gastrointestinal repair, there is, at present, an emphasis on their adhesion properties, a concern that often leads to the challenges posed by difficult-to-heal wounds and immune microenvironment regulation being overlooked. These limitations underscore an unmet clinical need and highlight the importance of developing novel therapeutic strategies for intestinal defect repair.

To address these challenges, in the present study we have developed a novel composite hydrogel that we have termed 'GEMA@PB', which integrates multiple properties suitable for intestinal repair, including compatibility with photo-crosslinkable 3D printing, enhanced repair capability, anti-inflammatory and antioxidant effects and wet-adhesion properties. This study has demonstrated that bioadhesive hydrogels, when used in 3D printing, offer substantial advantages for intestinal repair, paving the way for innovative applications in tissue engineering and regenerative medicine, and laying a foundation for future clinical applications.

Mussel-inspired adhesive materials have attracted significant attention due to their wet-adhesion properties [37]. The catechol groups in DA exhibit high reactivity, enabling strong covalent and non-covalent interactions with biological tissues, thereby providing superior wet adhesion, especially in aqueous environments. Zhang et al. [38] successfully developed a high-wet-adhesion hydrogel crosslinked from sodium alginate-DA, chondroitin sulfate and regenerated silk fibroin, which promoted endogenous cell recruitment and cartilage defect regeneration. In the present study, this adhesion principle was leveraged to fabricate the GEMA@PB composite hydrogel, where adhesion was achieved through catechol group reactions following 3D printing and molding. Initially, GDMA was prepared and mixed with dSI-ECMMA to form a solution, which was subsequently loaded with PBNPs to produce the GEMA@PB composite hydrogel. This GEMA@PB hydrogel is a dual-network composite, where GDMA and dSI-ECMMA exhibit photosensitivity. Through photo-crosslinking, GDMA and dSI-ECMMA form a dual-network structure, with PB dispersed within the network via hydrogen-bonding.

Hydrogels are ideal scaffolds in tissue engineering due to their permeability, tunable mechanical properties and compatibility with biological systems [39]. In recent years, 3D-printed hydrogel scaffolds have garnered widespread attention in tissue engineering [40]. These scaffolds often employ modified natural biopolymers, such as methacrylated hyaluronic acid (HAMA) [41], methacrylated silk fibroin (SIMA) [42] and methacrylated sodium alginate (ALGMA) [43]. However, hydrogels derived from natural biopolymers often demonstrate limited mechanical performance, repair capabilities and immunoregulatory functions when applied to intestinal repair. dSI-ECM retains its complex hierarchical structure and essential biological components, including proteins, polysaccharides, collagen and growth factors, making it an ideal candidate for tissue repair and regeneration [44]. Although previous studies have investigated the application of dSI-ECM in tissue repair, the key active components and biological functions have yet to be properly elucidated [45,46]. The present study has identified several key proteins in dSI-ECM, including COL6A1, COL6A2, COL6A3, LAMC1 and COL1A1, which serve crucial roles in cell differentiation, migration, adhesion and angiogenesis, providing a foundation for the further exploration of these proteins' roles.

The application of nanomaterials in hydrogels significantly enhances their mechanical propertie [47], making them more suitable for supporting heavily loaded tissues, or to be used in dynamic stress environments. Additionally, nanomaterials impart anti-inflammatory properties [48], which are critical in biomedical applications such as wound dressings, cartilage repair and artificial tissue substitutes. The present study has also revealed that the tensile strength and Young's modulus of the GEMA@PB group were superior to those of the GDMA and GEMA groups (Fig. 4C and D). Moreover, cell viability in the GEMA@PB group was higher compared with that in the GEMA and GDMA groups. This finding suggested that incorporating PBNPs led to a significantly improvement in the hydrogel's mechanical strength, effectively preventing leakage. Previous studies have shown that PBNPs possess notable anti-inflammatory properties, both promoting M2 macrophage polarization and downregulating pro-inflammatory cytokines, such as interleukin (IL)-1β and tumor necrosis factor-α (TNF-α), while upregulating anti-inflammatory cytokines such as IL-10 [1,49]. In the present study, using a lipopolysaccharide-induced macrophage inflammation model, we observed that the GEMA@PB group exhibited significantly reduced pro-inflammatory cytokine levels and increased levels of anti-inflammatory cytokine expression, suggesting that GEMA loaded with PBNPs effectively suppresses inflammation and promotes macrophage polarization towards the M2 phenotype. Although M2 macrophages play a critical role in tissue repair, excessive polarization can lead to fibrosis due to excessive extracellular matrix deposition. To mitigate this risk, the GEMA@PB hydrogel is designed to regulate on-demand PBNPs release, ensuring a controlled reduction of oxidative stress and inflammation without inducing persistent macrophage activation. The photo-crosslinked hydrogel network provides a gradual and sustained release profile, which prevents excessive immune modulation and allows for natural immune resolution during tissue regeneration. This controlled immune response fosters a balanced repair environment, minimizing the risk of fibrosis while maintaining effective intestinal defect healing.

Compared with traditional bioprinting techniques, in situ 3D bioprinting offers a unique approach by directly printing bioinks at the injury site, reducing the need for secondary implantation and enhancing integration with surrounding tissues. Several recent studies have explored in situ 3D bioprinting for skin, bone, and intestinal defect repair, demonstrating its feasibility and therapeutic potential [50–52]. Our study contributes to this growing field by developing a novel in situ 3D-bioprinted GDMA@PB nanozyme hydrogel, which exhibits wet adhesion and promotes macrophage phenotype modulation for intestinal defect repair.

To further elucidate the underlying mechanisms through which the composite hydrogel promotes intestinal repair, comprehensive mRNA sequencing-based analyses were conducted to examine the early-stage mRNA expression profiles during intestinal repair with the hydrogel. Various bioinformatics approaches subsequently revealed that the differentially expressed genes are primarily involved in immune regulation and inflammatory response processes (Fig. 9). Notably, our composite hydrogel demonstrated favorable outcomes in macrophage modulation. Based on the RNA-seq results, we hypothesized that the multifunctional hydrogel is able to facilitate the macrophage transition from the M1 to M2 phenotype. Additionally, early-tissue immunofluorescence staining indicated that, compared with the suture and GEMA groups, the GEMA@PB group exhibited significantly higher levels of CD31 and CD206 expression, and a lower level of CD86 expression (Fig. 9), suggesting that PBNPs enhance intestinal angiogenesis, reduce macrophage infiltration during the inflammatory phase, and inhibit pro-inflammatory cytokine secretion, potentially shortening the inflammatory stage and effectively promoting wound healing. These findings are consistent with those of previous studies, and further confirm the role of PBNPs in enhancing the mechanical strength and anti-inflammatory properties of biomaterials. These findings are consistent with those of previous studies, and further confirm the role of PBNPs in enhancing the mechanical strength and anti-inflammatory properties of biomaterials [53]. In summary, the present study has underscored the potential of 3D

printing technology in developing multifunctional biomaterials. Through integrating wet adhesion, antioxidant and biological repair functions, our hydrogel materials have paved the way for new applications in tissue engineering and regenerative medicine, thereby establishing a solid foundation for future clinical applications.

Despite the promising results, this study has certain limitations. The dual-sided adhesion of GEMA@PB hydrogel may lead to unintended adhesion to the peritoneum or other organs, which could pose risks in clinical applications. Future research will focus on material modifications to achieve single-sided adhesion, thereby improving targeted application in intestinal repair. Additionally, our study utilized rat models, which, while providing essential insights, do not fully replicate the human intestinal environment. Further preclinical trials in larger animal models, such as pigs and rhesus monkeys, are needed to evaluate the safety, biocompatibility, and long-term effects of the hydrogel in more clinically relevant conditions. Beyond intestinal defects, GEMA@PB hydrogel holds significant potential for broader clinical applications, including inflammatory bowel disease (IBD), ischemic bowel injury, anastomotic leakage, and radiation-induced intestinal damage. However, challenges related to scalability, regulatory compliance, and personalized adaptability must be addressed to facilitate clinical translation. Future directions include modifying the hydrogel for controlled adhesion, incorporating bioactive molecules to enhance tissue regeneration, and developing minimally invasive delivery strategies for improved clinical use. These advancements will be crucial for optimizing the therapeutic potential of GEMA@PB hydrogel and establishing its role in intestinal regenerative medicine.

5. Conclusion

In conclusion, the present study has successfully developed a novel multifunctional composite hydrogel that we have termed GEMA@PB, which is specifically designed to address the challenges of intestinal repair and regeneration. The GEMA@PB hydrogel, optimized for use with photo-crosslinkable 3D printing, demonstrated excellent repair capabilities, anti-inflammatory and wet-adhesion properties, making it particularly suitable for applications in dynamic biological environments. The incorporation of PBNPs not only enhanced the hydrogel's mechanical properties, but also provided significant anti-inflammatory effects through promoting M2 macrophage polarization and reducing pro-inflammatory cytokine expression. The results of the present study have demonstrated that GEMA@PB can effectively improve wound healing, as demonstrated by enhanced angiogenesis and reduced macrophage infiltration during the inflammatory phase in the *in vivo* model. This study has also underscored the potential of combining advanced materials science with bioengineering techniques to develop next-generation biomaterials for tissue engineering and regenerative medicine. The effectiveness of the GEMA@PB hydrogel that has been demonstrated in preclinical models lays a solid foundation for future clinical applications, offering a promising solution to the current limitations in gastrointestinal repair materials.

CRediT authorship contribution statement

Yang Su: Writing – original draft, Visualization, Validation, Supervision, Funding acquisition, Formal analysis, Data curation, Conceptualization. **Jingyi Ju:** Validation, Software, Formal analysis, Data curation. **Chentao Shen:** Investigation, Formal analysis. **Yanqi Li:** Formal analysis, Data curation. **Wangshuo Yang:** Formal analysis, Data curation. **Xuelai Luo:** Supervision. **Zhenxing Wang:** Supervision, Funding acquisition. **Jinhao Zeng:** Writing – review & editing, Funding acquisition, Data curation, Conceptualization. **Lu Liu:** Writing – review & editing, Supervision, Software, Project administration, Data curation, Conceptualization.

Declaration of Competing interest

The authors report no conflicts of interest in this work.

Appendix A. Supplementary data

Supplementary data to this article can be found online at https://doi.org/10.1016/j.mtbio.2025.101636.

Data availability

Data will be made available on request.

References

[1] J. Crippa, C. Magistro, I. Montroni, et al., Charting connections: a systematic review of colorectal surgery research networks, Eur. J. Surg. Oncol. 50 (6) (2024) 108322.

[2] A. Jessernig, A. Anthis, E. Vonna, et al., Early detection and monitoring of anastomotic leaks via naked eye-readable, non-electronic macromolecular network sensors, Adv. Sci. 11 (29) (2024) e2400673.

[3] M. Aker, A. Askari, M. Rabie, et al., Management of anastomotic leaks after elective colorectal resections: the East of England experience. A retrospective cohort, Int. J. Surg. 96 (2021) 106167.

[4] J. Steger, A. Jell, S. Ficht, et al., Systematic review and meta-analysis on colorectal anastomotic techniques, Ther Clin Risk Manag 18 (2022) 523–539.

[5] A. Setiawati, D. Jang, D. Cho, et al., An accelerated wound-healing surgical suture engineered with an extracellular matrix, Adv Healthc Mater 10 (6) (2021) e2001686.

[6] A.Y. Lee, J.Y. Cho, Clinical diagnostic advances in intestinal anastomotic techniques: hand suturing, stapling, and compression devices, World J. Gastrointest. Surg. 16 (5) (2024) 1231–1234.

[7] Y. Zhang, J. Cao, M. Lu, et al., A biodegradable magnesium surgical staple for colonic anastomosis: in vitro and in vivo evaluation, Bioact. Mater. 22 (2023) 225–238.

[8] T. Deng, D. Gao, X. Song, et al., A natural biological adhesive from snail mucus for wound repair, Nat. Commun. 14 (1) (2023) 396.

[9] M. Lo Presti, G. Rizzo, G.M. Farinola, F.G. Omenetto, Bioinspired biomaterial composite for all-water-based high-performance adhesives, Adv. Sci. 8 (16) (2021) e2004786.

[10] X. Liu, Y. Yang, H. Yu, et al., Instant and tough adhesives for rapid gastric perforation and traumatic pneumothorax sealing, Adv Healthc Mater 11 (23) (2022) e2201798.

[11] M. Li, R. Wei, C. Liu, et al., A "T.E.S.T." hydrogel bioadhesive assisted by corneal cross-linking for in situ sutureless corneal repair, Bioact. Mater. 25 (2023) 333–346.

[12] H. Yuk, C.E. Varela, C.S. Nabzdyk, et al., Dry double-sided tape for adhesion of wet tissues and devices, Nature 575 (7781) (2019) 169–174.

[13] J. Wu, H. Yuk, T.L. Sarrafian, et al., An off-the-shelf bioadhesive patch for sutureless repair of gastrointestinal defects, Sci. Transl. Med. 14 (630) (2022) eabh2857.

[14] J. Yu, Y. Qin, Y. Yang, et al., Robust hydrogel adhesives for emergency rescue and gastric perforation repair, Bioact. Mater. 19 (2023) 703–716.

[15] J. Snyder, C.M. Wang, A.Q. Zhang, et al., Materials and microenvironments for engineering the intestinal epithelium, Ann. Biomed. Eng. 48 (7) (2020) 1916–1940.

[16] S. Fre, M. Huyghe, P. Mourikis, S. Robine, D. Louvard, S. Artavanis-Tsakonas, Notch signals control the fate of immature progenitor cells in the intestine, Nature 435 (7044) (2005) 964–968.

[17] Y. Li, M.X. Hu, M. Yan, et al., Intestinal models based on biomimetic scaffolds with an ECM micro-architecture and intestinal macro-elasticity: close to intestinal tissue and immune response analysis, Biomater. Sci. 11 (2) (2023) 567–582.

[18] J. Li, X. Jiang, H. Li, M. Gelinsky, Z. Gu, Tailoring materials for modulation of macrophage fate, Adv Mater 33 (12) (2021) e2004172.

[19] J. Li, J. Song, Z. Deng, et al., Robust reactive oxygen species modulator hitchhiking yeast microcapsules for colitis alleviation by trilogically intestinal microenvironment renovation, Bioact. Mater. 36 (2024) 203–220.

[20] J. Chen, J.S. Caserto, I. Ang, et al., An adhesive and resilient hydrogel for the sealing and treatment of gastric perforation, Bioact. Mater. 14 (2022) 52–60.

[21] H. Fang, J. Ju, L. Chen, et al., Clay sculpture-inspired 3D printed microcage module using bioadhesion assembly for specific-shaped tissue vascularization and regeneration, Adv. Sci. 11 (21) (2024) e2308381.

[22] N. Petrić Howe, S. Bundell, A mussel-inspired glue for more sustainable sticking, Nature (2023).

[23] W. Kim, G.H. Kim, An intestinal model with a finger-like villus structure fabricated using a bioprinting process and collagen/SIS-based cell-laden bioink, Theranostics 10 (6) (2020) 2495–2508.

[24] Y. Zhao, H. Peng, L. Sun, et al., The application of small intestinal submucosa in tissue regeneration, Mater Today Bio 26 (2024) 101032.

[25] X. Tian, T. Fan, W. Zhao, et al., Recent advances in the development of nanomedicines for the treatment of ischemic stroke, Bioact. Mater. 6 (9) (2021) 2854–2869.

[26] L. Zhang, Z. Qin, H. Sun, et al., Nanoenzyme engineered neutrophil-derived exosomes attenuate joint injury in advanced rheumatoid arthritis via regulating inflammatory environment, Bioact. Mater. 18 (2022) 1–14.

[27] J. Zhao, X. Cai, W. Gao, et al., Prussian blue nanozyme with multienzyme activity reduces colitis in mice, ACS Appl. Mater. Interfaces 10 (31) (2018) 26108–26117.

[28] P. Jain, H. Kathuria, N. Dubey, Advances in 3D bioprinting of tissues/organs for regenerative medicine and in-vitro models, Biomaterials 287 (2022) 121639, https://doi.org/10.1016/j.biomaterials.2022.121639.

[29] S. Kim, S. Min, Y.S. Choi, et al., Tissue extracellular matrix hydrogels as alternatives to Matrigel for culturing gastrointestinal organoids, Nat. Commun. 13 (1) (2022) 1692.

[30] X. Cai, W. Gao, M. Ma, et al., A prussian blue-based core-shell hollow-structured mesoporous nanoparticle as a smart theranostic agent with ultrahigh pH-responsive longitudinal relaxivity, Adv Mater 27 (41) (2015) 6382–6389.

[31] Z. Li, Z. Chen, H. Chen, et al., Polyphenol-based hydrogels: pyramid evolution from crosslinked structures to biomedical applications and the reverse design, Bioact. Mater. 17 (2022) 49–70.

[32] D.M. Mosser, K. Hamidzadeh, R. Goncalves, Macrophages and the maintenance of homeostasis, Cell. Mol. Immunol. 18 (3) (2021) 579–587.

[33] J.H. Hageman, M.C. Heinz, K. Kretzschmar, J. van der Vaart, H. Clevers, H. Snippert, Intestinal regeneration: regulation by the microenvironment, Dev. Cell 54 (4) (2020) 435–446.

[34] X. Xue, D.M. Falcon, The role of immune cells and cytokines in intestinal wound healing, Int. J. Mol. Sci. 20 (23) (2019) 6097.

[35] N.D. Brown, E.E. Vomhof-DeKrey, Focal adhesion kinase and colony stimulating factors: intestinal homeostasis and innate immunity crosstalk, Cells 13 (14) (2024) 1178.

[36] M. Winter, B. Heitplatz, N. Koppers, et al., The impact of phase-specific macrophage depletion on intestinal anastomotic healing, Cells 12 (7) (2023) 1039.

[37] C. Zhang, B. Wu, Y. Zhou, F. Zhou, W. Liu, Z. Wang, Mussel-inspired hydrogels: from design principles to promising applications, Chem. Soc. Rev. 49 (11) (2020) 3605–3637.

[38] F.X. Zhang, P. Liu, W. Ding, et al., Injectable Mussel-Inspired highly adhesive hydrogel with exosomes for endogenous cell recruitment and cartilage defect regeneration, Biomaterials 278 (2021) 121169.

[39] M.H. Norahan, S.C. Pedroza-González, M.G. Sánchez-Salazar, M.M. Álvarez, G. Trujillo de Santiago, Structural and biological engineering of 3D hydrogels for wound healing, Bioact. Mater. 24 (2023) 197–235.

[40] Y. Yang, W. Wang, Q. Zeng, et al., Fabricating oxygen self-supplying 3D printed bioactive hydrogel scaffold for augmented vascularized bone regeneration, Bioact. Mater. 40 (2024) 227–243.

[41] Y. Fan, Z. Yue, E. Lucarelli, G.G. Wallace, Hybrid printing using cellulose nanocrystals reinforced GelMA/HAMA hydrogels for improved structural integration, Adv Healthc Mater 9 (24) (2020) e2001410.

[42] S.H. Kim, H. Hong, O. Ajiteru, et al., 3D bioprinted silk fibroin hydrogels for tissue engineering, Nat. Protoc. 16 (12) (2021) 5484–5532.

[43] J. Wang, Y. Wu, G. Li, et al., Engineering large-scale self-mineralizing bone organoids with bone matrix-inspired hydroxyapatite hybrid bioinks, Adv Mater 36 (30) (2024) e2309875.

[44] Y.T. Song, Y.Q. Li, M.X. Tian, et al., Application of antibody-conjugated small intestine submucosa to capture urine-derived stem cells for bladder repair in a rabbit model, Bioact. Mater. 14 (2022) 443–455.

[45] G.G. Giobbe, C. Crowley, C. Luni, et al., Extracellular matrix hydrogel derived from decellularized tissues enables endodermal organoid culture, Nat. Commun. 10 (1) (2019) 5658.

[46] Y. Jiang, L.L. Zhang, F. Zhang, et al., Dual human iPSC-derived cardiac lineage cell-seeding extracellular matrix patches promote regeneration and long-term repair of infarcted hearts, Bioact. Mater. 28 (2023) 206–226.

[47] M. Zhang, F. Xu, J. Cao, Q. Dou, J. Wang, J. Wang, L. Yang, W. Chen, Research advances of nanomaterials for the acceleration of fracture healing, Bioact. Mater. 31 (2024) 368–394.

[48] S. Wang, Y. Liu, Q. Sun, et al., Triple cross-linked dynamic responsive hydrogel loaded with selenium nanoparticles for modulating the inflammatory microenvironment via PI3K/akt/NF-κB and MAPK signaling pathways, Adv. Sci. 10 (31) (2023) e2303167.

[49] H. Oh, D. Son, J.S. Lee, et al., Reactive oxygen species scavenging nanofibers with chitosan-stabilized Prussian blue nanoparticles for enhanced wound healing efficacy, Int. J. Biol. Macromol. 219 (2022) 835–843.

[50] M. Shen, L. Wang, Y. Gao, L. Feng, C. Xu, S. Li, X. Wang, Y. Wu, Y. Guo, G. Pei, 3D bioprinting of in situ vascularized tissue engineered bone for repairing large segmental bone defects, Mater Today Bio 16 (2022) 100382, https://doi.org/10.1016/j.mtbio.2022.100382.

[51] M.T. Thai, P.T. Phan, H.A. Tran, C.C. Nguyen, T.T. Hoang, J. Davies, J. Rnjak-Kovacina, H.P. Phan, N.H. Lovell, T.N. Do, Advanced soft robotic system for in situ 3D bioprinting and endoscopic surgery, Adv. Sci. 10 (12) (2023) e2205656, https://doi.org/10.1002/advs.202205656.

[52] M. Zhao, J. Wang, J. Zhang, J. Huang, L. Luo, Y. Yang, K. Shen, T. Jiao, Y. Jia, W. Lian, J. Li, Y. Wang, Q. Lian, D. Hu, Functionalizing multi-component bioink with platelet-rich plasma for customized in-situ bilayer bioprinting for wound healing, Mater Today Bio 16 (2022) 100334, https://doi.org/10.1016/j.mtbio.2022.100334.

[53] Q. Guo, T. Yin, W. Huang, R. Nan, T. Xiang, S. Zhou, Hybrid hydrogels for immunoregulation and proangiogenesis through mild heat stimulation to accelerate whole-process diabetic wound healing, Adv Healthc Mater 13 (18) (2024) e2304536.